Astronomy & Astrophysics

A second view on the X-ray polarization of NGC 4151 with IXPE

V. E. Gianolli[1,2],⋆ , S. Bianchi[2] , E. Kammoun[2] , A. Gnarini[2] , A. Marinucci[3] , F. Ursini[2] , M. Parra[1,2] ,
A. Tortosa[4] , A. De Rosa[5] , D. E. Kim[5,6,7] , F. Marin[8] , G. Matt[2] , R. Serafinelli[4] , P. Soffitta[5] ,
D. Tagliacozzo[2] , L. Di Gesu[3] , C. Done[9,10] , H. L. Marshall[11] , R. Middei[5,12] , R. Mikusincova[5] ,
P-O. Petrucci[1] , S. Ravi[11] , J. Svoboda[13] , and F. Tombesi[7,14,15]

(Affiliations can be found after the references)

ABSTRACT

We report on the second observing program of the active galactic nucleus NGC 4151 with simultaneous Imaging X-ray Polarimetry Explorer (IXPE; 750 ks), *NuSTAR* (∼60 ks), *XMM-Newton* (∼75 ks), and NICER (∼65 ks) pointings. NGC 4151 is the first Type-1 radio-quiet Seyfert galaxy with constrained polarization properties for the X-ray corona. Despite the lower flux state in which the source was re-observed and the resulting higher contribution of the constant reflection component in the IXPE energy band, our results are in agreement with the first detection. From polarimetric analysis, a polarization degree $\Pi = 4.7 \pm 1.3\%$ and polarization angle $\Psi = 77° \pm 8°$ east of north (68% c.l.) were derived in the 2.0–8.0 keV energy range. Combining the two observations leads to polarization properties that are more constrained than those of the individual detections, showing $\Pi = 4.5 \pm 0.9\%$ and $\Psi = 81° \pm 6°$ (with a detection significance of ∼4.6σ). The observed polarization angle aligns very well with the radio emission in this source, supporting, together with the significant polarization degree, a slab or wedge geometry for the X-ray corona. However, a switch in the polarization angle at low energies (37° ± 7° in the 2–3.5 keV bin) suggests the presence of another component. When it is included in the spectro-polarimetric fit, a high polarization degree disfavors an interpretation in terms of a leakage through the absorbers, instead pointing to scattering from some kind of mirror.

Key words. polarization – galaxies: active – galaxies: individual: NGC 4151 – galaxies: Seyfert

1. Introduction

X-ray polarimetry has emerged as a powerful tool in unveiling the geometry of one of the innermost and most enigmatic regions of active galactic nuclei (AGN): the X-ray corona. According to the Unified Model of AGN, the corona is composed of hot (with a typical temperature of $kT_e \simeq$ 10–100 keV, e.g., Fabian et al. 2015, 2017; Tortosa et al. 2018) and rarefied optically thin electron plasma situated in the innermost region of the accretion flow. This region up-scatters the UV photons emitted by the disk, producing the primary X-ray emission (Sunyaev & Titarchuk 1980; Zdziarski et al. 2000). The polarization signal of the coronal emission is very sensitive to the geometry of the scattering material (e.g., Schnittman & Krolik 2010; Tamborra et al. 2018; Zhang et al. 2019; Marinucci et al. 2022; Ursini et al. 2022; Gianolli et al. 2023; Ingram et al. 2023; Tagliacozzo et al. 2023). Multiple studies on the physical properties of the X-ray corona (i.e., the optical depth τ and the electron temperature kT_e, Shapiro et al. 1976) have been performed (e.g., Petrucci et al. 2001; Matt et al. 2015; Ricci et al. 2018; Tortosa et al. 2018; Kamraj et al. 2022; Kang & Wang 2022; Serafinelli et al. 2024, and references therein). However, only with the launch of the Imaging X-ray Polarimeter Explorer (IXPE; Weisskopf et al. 2022) mission together with its synergy with simultaneous observations of the Nuclear Spectroscopic Telescope Array Mission (*NuSTAR*) and the X-ray Multi-Mirror Mission (*XMM-Newton*) have new insights been obtained on the geometry of this region in Type-1 AGN (Gianolli et al. 2024; Marin et al. 2024).

One of the X-ray brightest Seyfert galaxies in the local Universe is NGC 4151. Intensively studied, it has shown different layers of absorption from both neutral and ionized gas (e.g., Beuchert et al. 2017; Gianolli et al. 2023). Archival observations of the source revealed significant spectral variability in the 1 − 6 keV range. Furthermore, the source shows transitions from optical Type 1.5 during high-flux states, where the AGN can reach a flux level as high as $F_{0.5−10\,keV} \sim 2.8 \times 10^{-10}$ erg s^{-1} cm^{-2}, to optical Type 1.8 during low-flux states ($F_{0.5−10\,keV} \sim 8.7 \times 10^{-11}$ erg s^{-1} cm^{-2}; see Antonucci & Cohen 1983; Shapovalova et al. 2012; Beuchert et al. 2017).

NGC 4151 is the first Type-1 radio-quiet AGN with constrained polarization properties for the X-ray corona. From polarimetric analysis, a polarization degree (PD) of $\Pi = 4.9 \pm 1.1\%$ (68% confidence level; c.l.) and a polarization angle (PA) of $\Psi = 86° \pm 7°$ have been measured with a significance above 99.99% (Gianolli et al. 2023, "G23" hereafter). Given that the primary X-ray emission was the dominant component in the IXPE energy band and the reflection, arising from the reprocessing of the primary continuum off surrounding material (such as the torus, as favored by the analysis in G23, or the accretion disk) and which contributed only up to 6%, the observed PD and PA refer to the primary continuum. When taken into account in the spectro-polarimetric analysis, and setting the primary continuum and reflection PAs to differ by 90 degrees, a PD = $7.7 \pm 1.5\%$ and PA = $87° \pm 6°$ for the X-ray primary emission are found. Numerical simulations in G23 show that, based on the observed X-ray polarization properties, a radially extended slab geometry is preferred for the corona. Interestingly, a further component with different polarization properties may be the cause of the observed change in polarization properties in the 2–3.5 keV

⋆ Corresponding author;
`vittoria.gianolli@univ-grenoble-alpes.fr`

band (PD = 4.3 ± 1.6% and PA = 42° ± 11°). Due to its high variability in the X-ray band, NGC 4151 is an excellent candidate for studying potential changes in the observed polarization properties.

In the following, we present the spectral and spectro-polarimetric analyses of the simultaneous IXPE, *NuSTAR*, and *XMM-Newton* data and the results of the Neutron Star Interior Composition Explorer (NICER; Gendreau et al. 2012; Arzoumanian et al. 2014; Gendreau et al. 2016) monitoring. The structure of this paper is as follows. In Sect. 2, we provide details on the observations and data reduction processes for IXPE, *XMM-Newton*, *NuSTAR*, and NICER. In Sect. 3, we present the findings of the polarimetric, spectral, and spectro-polarimetric analyses. In Sect. 4 the results are discussed.

2. Observing campaign and data reduction

The second IXPE observation of NGC 4151 was performed during the first cycle of the IXPE General Observer program.[1] Due to the long exposure time (750 ks), it has been divided into two segments: 23–28 April and 15–26 May, 2024. We used the level two event files, which are calibrated adopting a standard IXPE pipeline from the Science Operation Center (SOC).[2] We applied the background rejection method following Di Marco et al. (2023)'s guidelines for faint sources. To extract the source (background) data in the three detector units (DUs), a 68″ circle (annulus with internal radius of 180″ and outer of 240″) was adopted. The source extraction radius was derived iteratively to maximize the signal-to-noise ratio in the 2.0–8.0 keV band, similar to the procedure described in Piconcelli et al. (2004). Any remaining background contribution was subtracted during the polarimetric analysis. Subsequently, to estimate the polarization properties, we employed two methods: (1) creating a polarization cube (PCUBE; using the IXPEOBSSIM software version 31.0.1; Baldini et al. 2022) and (2) generating *I*, *Q*, and *U* spectra using XSELECT (from the HEASOFT package version 6.33.2; NASA Heasarc 2014), considering the weighted analysis method with the parameters stokes=Neff (Di Marco et al. 2022). Both methods adopt the latest available calibration file, specifically version 13 (20240101) in IXPEOBSSIM and CALDB 20240125 for XSELECT. The Ancillary Response File (ARF) and Modulation Response File (MRF) for each detector unit were generated using the ixpecalcarf task and considering the same extraction radius used for the source region. The results from the model-independent polarization analysis using PCUBE are presented in Sect. 3.1, whereas the *I*, *Q*, and *U* spectra are adopted in Sect. 3.3 for the spectro-polarimetric analysis.

To constrain the physical properties of the X-ray corona and disentangle the contribution of each spectral component, we requested simultaneous *NuSTAR* and *XMM-Newton* observations. However, due to a *NuSTAR* star tracker blockage for the target and other time-constrained *NuSTAR* and *XMM* observations during the second window of the scheduled IXPE observation, both observations were divided into two pointings.

XMM-Newton observed NGC 4151 on May 21-22 ("X1" hereafter) and on May 24-25 ("X2" hereafter), 2024, for 14 ks and 25 ks (effective exposure times after filtering process) of exposure time using the EPIC-pn (Strüder et al. 2001). For both

observations, the source and background spectra were extracted following G23 extraction radii. A correction for the effective area was applied using the Science Analysis Software (SAS) keyword, APPLYABSFLUXCORR, specifically designed to improve consistency with simultaneous *NuSTAR* data.

The *NuSTAR* (Harrison et al. 2013) observations were carried out from May 22 to 23 ("N1" hereafter) and from May 25 to 27 ("N2" hereafter), 2024, adopting both coaligned X-ray telescopes equipped with Focal Plane Module A (FPMA) and B (FPMB). The Nupipeline task was employed alongside the latest calibration files from the database (CALDB 20221229) to generate and calibrate cleaned event files. The extraction radii for the source and background were set to be the same as those adopted by G23, namely, 2′and 1.22′. The net exposure times for FPMA and FPMB during N1 are 25 and 24 ks, while for N2 the values are 34 and 33 ks. As found in the previous campaign, significant deviations from the pn spectrum are still present in the *NuSTAR* spectra below 4 keV. Hence, we considered *NuSTAR* data as only above 4 keV (see, e.g., G23). We accounted for an energy shift of around 2000 km s^{-1} at the iron line using vashift to address lingering calibration issues, which have also been observed in the past (Gianolli et al. 2023; Ingram et al. 2023; Serafinelli et al. 2023).

Given that the coverage of *XMM* and *NuSTAR* observations is limited to the second IXPE observing window and due to the highly variable nature of NGC 4151, it is essential to track its absorption and flux states also during the first segment. Hence, we requested daily monitoring of the source with *NICER* from April 22 to 30, 2024, for a total of ∼35 ks. The NICER data were also collected between May 1 and 14 (other ∼30 ks), allowing us to check for any changes during the time frame between each IXPE pointing.

The NICER unfiltered data events were reprocessed using the nicerl2 tool included in the HEASoft software package using the latest software and calibration files (February, 27, 2024). We applied the nicerl3-spect task to the clean event files and obtain the spectra. For the background, we used the SCORPEON model, which includes contributions from many physically motivated components. It takes into account sky-related components such as the cosmic X-ray background, local hot bubble, and galactic halo as well as non-X-ray background components such as cosmic rays, the South Atlantic Anomaly, trapped electrons, precipitating electrons, and low-energy storm-related electrons.

The extracted spectra were binned following the method of Kaastra & Bleeker (2016). All uncertainties are provided at a 68% (1σ) c.l., unless otherwise specified, and upper and lower limits are reported at a 99% (2.6σ) c.l. for one single parameter. Throughout our analysis, we considered a redshift of $z = 0.003326$ (Wolfinger et al. 2013) along with cosmological parameters $H_0 = 70$ km s^{-1} Mpc^{-1}, $\Lambda_0 = 0.73$, and $\Lambda_m = 0.27$.

3. Data analysis

3.1. IXPE polarimetric analysis

We report the results of the unweighted PCUBE analysis on the second IXPE observation of NGC 4151. For the two segments separately, we obtained in the 2.0–8.0 keV energy band (from the three combined DUs), after background subtraction, only an upper limit for the PD (i.e., $\Pi < 7.8\%$) in the first segment and a significant detection (with $\Pi = 5.4 \pm 1.6\%$ and PA $\Psi = 78° \pm 8°$) in the second. Given the consistency of the PDs in the two segments, we proceeded by summing them together,

Table 1. Polarization parameters of the first, second, and a combination of the two IXPE observations for different energy bands.

Obs	Energy range [keV]	$\Pi \pm 1\sigma$ [%]	$\Psi \pm 1\sigma$ [deg]
1st	2.0–8.0	4.6 ± 1.2	85 ± 8
	2.0–3.5	4.2 ± 1.6	40 ± 11
	3.5–5.0	4.9 ± 1.4	99 ± 8
	5.0–8.0	6.7 ± 2.0	87 ± 9
2nd	2.0–8.0	4.7 ± 1.3	77 ± 8
	2.0–3.5	5.2 ± 1.7	34 ± 10
	3.5–5.0	3.1 ± 1.5	96 ± 14
	5.0–8.0	8.2 ± 2.2	81 ± 8
Combined	2.0–8.0	4.5 ± 0.9	81 ± 6
	2.0–3.5	4.6 ± 1.1	37 ± 7
	3.5–5.0	4.0 ± 1.0	98 ± 7
	5.0–8.0	7.2 ± 1.4	84 ± 6

finding $\Pi = 4.7 \pm 1.3\%$ and $\Psi = 77° \pm 8°$, with a detection significance at a 99.84% c.l. ($\sim 3.2\sigma$). In Table 1 (middle part), we show the Π and Ψ obtained in the three energy bands adopted in G23: 2.0–3.5, 3.5–5.0, and 5.0–8.0 keV. We found a significant detection only for the last energy bin (at $\sim 3.3\sigma$), whereas we found marginal detections for the first and middle bins (at $\sim 2.6\sigma$ and $\sim 1.2\sigma$, respectively).

To compare the results of the second observation with those of the first, we also re-extracted the PCUBE of the first observation, adopting the new calibration files available in IXPEOBSSIM. We report the derived polarization properties in Table 1 (upper part). In the left panel of Figure 1, we present a comparison between the polarization contours of the first and second detections in the full energy band of IXPE. Meanwhile, in the right panels of Figure 1, we show the polarization contours obtained for the three energy bins in the first and second observations. We observed that the polarization properties of the second observation (for both the 2.0–8.0 keV energy band and the individual bins) are always well consistent with those found during the first detection. Hence, we combined the PCUBE of both observations. In Fig. 2, we report the contours of the polarimetric properties obtained in the full energy band and for the three bins. We observed that once the two observations are combined together, all PDs and PAs are more constrained than in the individual observations. In particular, for the full energy band of IXPE, we obtained $\Pi = 4.5 \pm 0.9\%$ and $\Psi = 81° \pm 6°$ (with detection significance $\sim 4.6\sigma$). For the three energy bins, we present in Table 1 the PDs, which are significantly detected (at $\sim 3.5\sigma$, $\sim 3.3\sigma$, and $\sim 4.5\sigma$, respectively) in each energy bin, and the PAs. In the second and combined observations, the peculiar behavior detected by G23 in the 2.0–3.5 keV energy bin remains evident, and a difference of $\sim 45°$ between the PA in this bin and that derived for the full band is present. Meanwhile, a difference of $\sim 60°$ is observed between the PAs of the 2.0–3.5 keV and 3.5–5.0 keV energy bins.

3.2. Spectral Analysis: XMM-Newton, NuSTAR, and NICER

To perform the spectral analysis of NGC 4151, we used XSPEC version 12.13.0 (Arnaud 1996), considering the 0.5–10.0 keV *XMM-Newton* and 4.0–79.0 keV *NuSTAR* spectra simultaneously. We show in Fig. 3 the *XMM* and *NuSTAR* spectra of the first and second observational campaigns. The spectra appear consistent below 1 keV and exhibit a

similar spectral shape at high energies. Most of the spectral variability is concentrated between 2.0 and 6.0 keV, suggesting variability in obscuration. Hence, given the complexity of modeling the X-ray spectrum of NGC 4151 (e.g., Weaver et al. 1994; Zdziarski et al. 1996; Yang et al. 2001; De Rosa et al. 2007; Kraemer et al. 2008; Lubiński et al. 2010; Gianolli et al. 2023), we adopted the same model used in G23: (tbabs)*(CLOUDY + zgauss + PC*PC*WA*(BORUS 1 + BORUS 2 + nthcomp)). We note that tbabs models the Galactic absorption, a thermally Comptonized continuum (nthcomp; Zdziarski et al. 1996; Życki et al. 1999) represents the primary X-ray emission, and BORUS (Baloković et al. 2018, 2019) is used for modeling the reflection component. Following the approach of G23, we separated the reflection component (i.e., the emission reprocessed by a torus) from the fluorescent lines by using specific BORUS tables. Soft X-ray emission was accounted for by incorporating a photoionized plasma emission component generated with CLOUDY (Ferland et al. 1998; Bianchi et al. 2010), and the residuals around the O VII emission line triplet were mitigated using a Gaussian line. The different layers of absorption (e.g., Keck et al. 2015; Gianolli et al. 2023) were modeled by two neutral partial-covers (PCs; zpcfabs) along with a warm absorber (WA; modeled with zxipcf and covering a factor fixed to one). The applied multiplicative constants (which accommodate cross-calibration uncertainties between FPM modules and EPIC-pn as well as marginal flux variability of the source, as the observations are not strictly simultaneous) are of the order of 1.20. The source was detected in an average flux state, with $F_{0.5-10\,keV} = 1.07(1.33) \times 10^{-10}$ erg s^{-1} cm^{-2} for X1+N1 (X2+N2), which is lower than the first campaign ($F_{0.5-10\,keV} = 1.73 \times 10^{-10}$ erg s^{-1} cm^{-2}).

As a first step of the spectral analysis, we analyzed the Fe Kα emission line by focusing on the 5.0–10.0 keV energy band. By doing so, we aimed at assessing the possible presence of a significant relativistic reflection component and the variability of the line. As found by G23 for the first campaign, NGC 4151 does not show a clear relativistic component in the new data, which is different from what has been found in some previous observations of the source (e.g., Yaqoob et al. 1995; Zoghbi et al. 2019, and references therein). The line can be modeled with a single Gaussian, but it is only slightly resolved ($\sigma \sim 60$–70 eV). We find no evidence of variability in the line parameters (intensity and width), either between X1+N1 and X2+N2 or with respect to the first campaign (Fig. 4). Consequently, the equivalent width of the iron line anti-correlates with the flux of the source, being EW = 150 ± 15 (126^{+10}_{-7}) eV in the X1+N1 (X2+N2) data and EW = 100 ± 6 eV in the 2022 data.

Subsequently, we considered the full broadband X1+N1 and X2+N2 data, and we fit them together with the *XMM+NuSTAR* data from the first campaign in order to identify any variability in the spectral components. We assumed that the reflection component did not change, as evidenced by the absence of variation in the Fe Kα emission line. Meanwhile, we allowed the photon index and the normalization of the primary continuum to vary. Furthermore, all absorbers (both neutral and ionized) show a significant variation between X1+N1 and the 2022 campaign, with only the first neutral PC (column density and covering factor) differing between X1+N1 and X2+N2 (see Table 2). We also observed a small but significant change for the parameters of the photoionized gas that models the soft X-ray emission, confirming a similar variability noted by Zoghbi et al. (2019). In the end, we obtained an acceptable best fit with χ^2/d.o.f = 5878/5208. We show the best fit parameters in Table 2 (those of the 2022 campaign are also reported) and the spectra with residuals in Fig. 3.
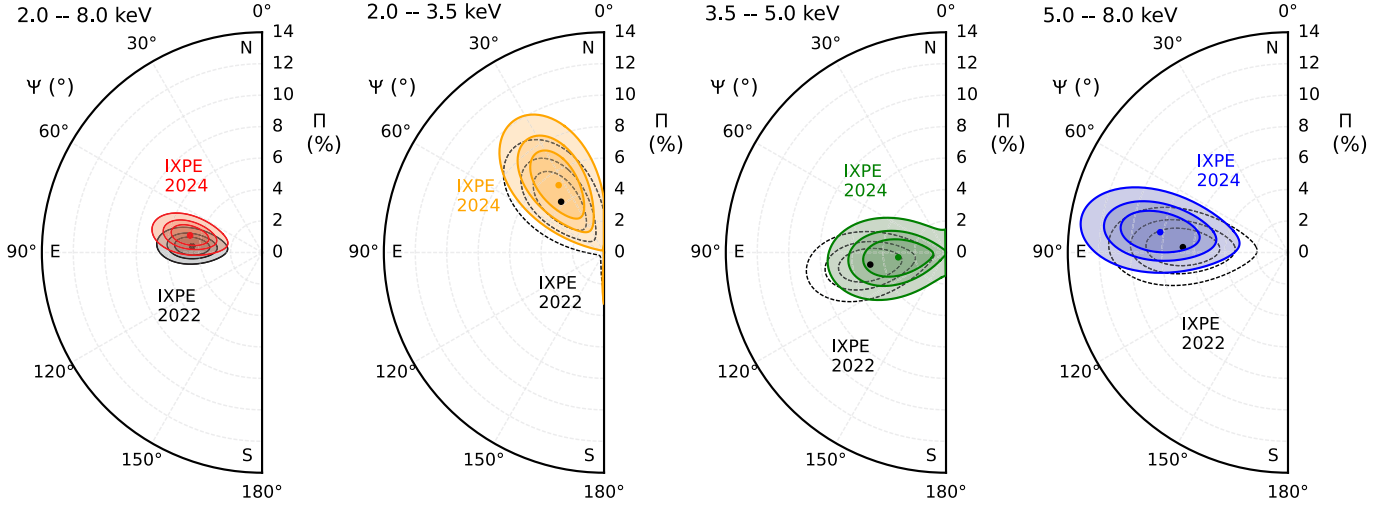
Fig. 1. Comparison between the first and second IXPE observations. The polarization contours are (68, 90, and 99% c.ls.; see Eq. (32) of Muleri 2022) for the PD Π and the PA Ψ with respect to the north direction. First left panel: Comparison between first (in black) and second (in red) observation considering IXPE full energy band. Second to fourth panels: Comparison between first and second observation considering the division in three energy bins. Colors refer to the 2.0–3.5 keV (black, the first observation; yellow, the second observation); 3.5–5.0 keV (black, the first observation; green, the second observation); and 5.0–8.0 keV (black, the first observation; blue, the second observation) energy ranges, respectively.
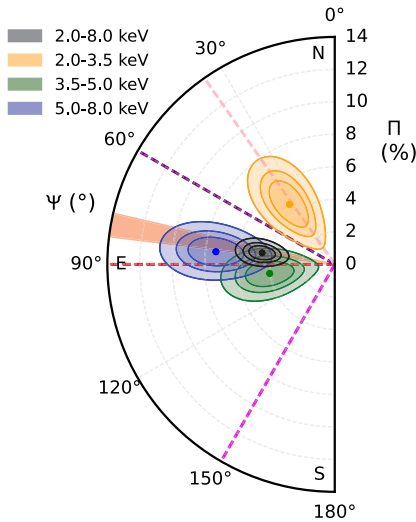
Fig. 2. First and second IXPE observations combined. Polarization contours (68, 90, and 99% c.ls.) for the PD Π and the PA Ψ with respect to the north direction. Colors refer to the 2.0–8.0 keV (in black), 2.0–3.5 keV (in yellow), 3.5–5.0 keV (in green), and 5.0–8.0 keV (in blue) energy ranges, respectively. The orange region shows the direction of the radio emission. The red, purple, and pink dashed lines represent the direction of the inner few pc of the radio jet, the narrow-line region, and an unclassified feature, respectively (see Sect. 4). The magenta dashed line shows the direction of the torus, which has been identified in X-rays with a position angle of ~150° (Wang et al. 2011), appearing to coincide with the H$_2$ region identified by Storchi-Bergmann et al. (2009). It is worth noting that the accretion disk axis could be misaligned with the torus by ~20° (May et al. 2020). Furthermore, Bentz et al. (2022) describe the broad-line region as a thick disk with a ~57° opening angle and a ~58° inclination angle, suggesting our view skims just above the broad-line region surface.

Whereas in G23, the reflection (reprocessed continuum and fluorescent lines) contribution was only about 6% in the 2.0–8.0 keV energy band, we find it to be 26% for X1+N1 and 21%
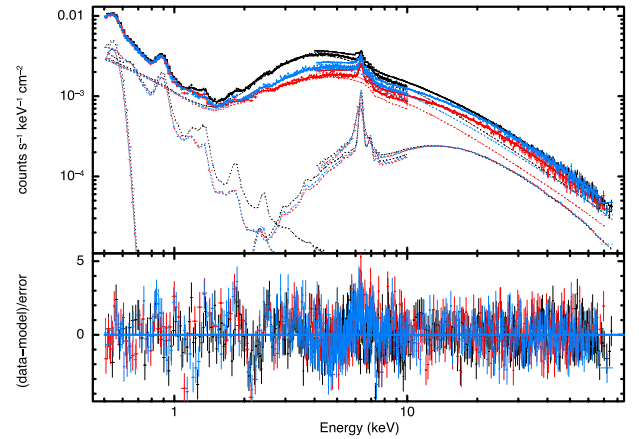

Fig. 3. *XMM-Newton* and *NuSTAR* spectra with residuals. The *XMM-Newton*/EPIC-pn and the grouped *NuSTAR* FPMA and FPMB of the first campaign are shown in black. In red, the *XMM-Newton*/EPIC-pn and the grouped *NuSTAR* FPMA and FPMB of the second campaign (first segments) are shown. In blue, the *XMM-Newton*/EPIC-pn and the grouped *NuSTAR* FPMA and FPMB of the second campaign (second segments) are presented.

for X2+N2. The contribution of the Fe Kα line is 8% (7%) in the 5.0–8.0 keV for the two new observations. We note that the observed trend is in agreement with our assumption on the constant reflection (which is justified via the iron line), namely as the flux increases (from X1+N1 to X2+N2 and up to the 2022 level), the contribution of the reflection decreases. Moreover, as also obtained in G23, the contribution of the photoionized emission in the 2–3.5 keV band is not significant and becomes so only at lower energies. On the other hand, the 2–3.5 keV band manifests an excess relative to the absorbed primary continuum, which has been interpreted in this model as the primary emission leakage through the partial-covers. Its contribution is around 15% (22%) in the X1+N1 (X2+N2) observation, becoming 7%

Table 2. Best fit from the spectral analysis.

Parameter	Value 1st obs	Value X1+N1	Value X2+N2
CLOUDY (Photoionized emitter)			
$\log U$	1.35 ± 0.01	$1.11^{+0.01}_{-0.02}$ [+]	
$\log(N_{\mathrm{H}} / \mathrm{cm}^{-2})$	21.63 ± 0.02	$21.54^{+0.01}_{-0.02}$ [+]	
PC 1 (Neutral absorber 1)			
$\log(N_{\mathrm{H}} / \mathrm{cm}^{-2})$	23.02 ± 0.01	23.27 ± 0.01	23.18 ± 0.01
Cf	0.78 ± 0.01	0.73 ± 0.01	0.75 ± 0.01
PC 2 (Neutral absorber 2)			
$\log(N_{\mathrm{H}} / \mathrm{cm}^{-2})$	22.64 ± 0.01	22.68 ± 0.01 [+]	
Cf	0.95 ± 0.01	0.93 ± 0.01 [+]	
WA (Warm absorber)			
$\log(N_{\mathrm{H}} / \mathrm{cm}^{-2})$	23.13 ± 0.03	$23.59^{+0.04}_{-0.05}$ [+]	
$\log(\xi / \mathrm{erg\,cm\,s}^{-1})$	4.12 ± 0.02	4.31 ± 0.03 [+]	
BORUS 1/2 (Neutral reflector 1/2)			
$\log(N_{\mathrm{H}} / \mathrm{cm}^{-2})$	24.45 ± 0.01	24.45 [*]	
$A_{\mathrm{Fe}}/A_{\mathrm{Fe},\odot}$	0.62 ± 0.01	0.62 [*]	
norm	0.09 ± 0.01	0.09 [*]	
nthcomp (Comptonized primary continuum)			
Γ	1.85 ± 0.01	1.88 ± 0.01	1.82 ± 0.01
kT_{e} [keV]	60^{+7}_{-6}	60 [*]	
norm	0.093 ± 0.001	0.067 ± 0.002	0.071 ± 0.001
χ^2/d.o.f.	$743/660$	$2556/2245$	$2576/2255$
$F_{2-10\,\mathrm{keV}} / [\times 10^{-10}\,\mathrm{erg\,cm}^{-2}\,\mathrm{s}^{-1}]$	1.680 ± 0.003	1.025 ± 0.004	1.277 ± 0.004
$L_{2-10\,\mathrm{keV}} / [\times 10^{42}\,\mathrm{erg\,s}^{-1}]$	4.060 ± 0.006	2.477 ± 0.010	3.085 ± 0.009

Notes. [*]: During X1+N1 and X2+N2 data fitting, we fixed these values to those obtained in G23 best fit (we report for the first observation the uncertainties obtained in G23). [+]: During data fitting, we fixed the values of X2+N2 to those obtained for X1+N1, as they do not vary when left free. Normalization in units of photons $\mathrm{s}^{-1}\,\mathrm{cm}^{-2}\,\mathrm{keV}^{-1}$. The best fit values are adopted in the spectro-polarimetric analysis.
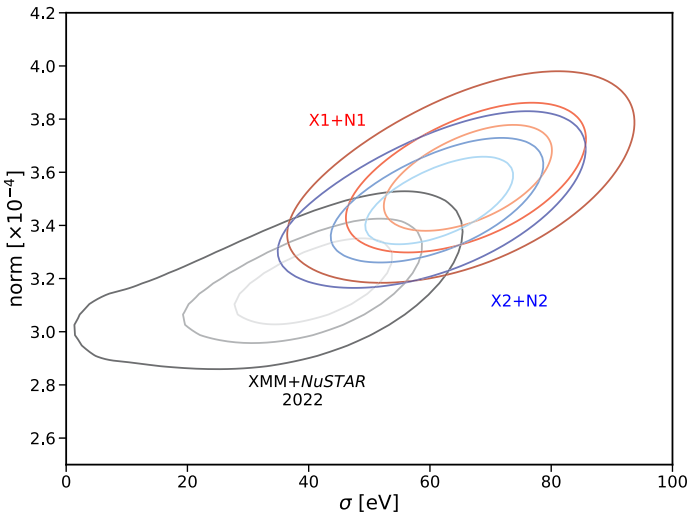

Fig. 4. Iron emission line: width versus normalization contour plots. Black refers to the 2022 data, red to the X1+N1 data, and blue to the X2+N2 data.

(8%) for X1+N1 (X2+N2) in the 3.5–5.0 keV and 2% (3%) for X1+N1 (X2+N2) in the 5.0–8.0 keV bin.

A total of 23 NICER observations were also performed continuously from the beginning of the first segment of IXPE until the beginning of the second. In Fig. 5, we report the variation of the 2.0–10.0 keV flux compared to the values observed during the past and new *XMM+NuSTAR*+IXPE campaigns. We note

that the six observations strictly simultaneous to the first segment of the new IXPE observation (see light green band on the left of Fig. 5) display a flux similar to that measured during X2+N2. We thus fit the six simultaneous pointings to monitor possible changes in the absorbers and continuum. We note that due to discrepancies between the NICER and *XMM* spectra below 1 keV and because this energy band is not crucial for our purposes, we only consider data above this energy. A good fit (χ^2/d.o.f. = 718/612) was obtained, allowing the normalization of the primary emission and the first neutral PC (column density and covering factor) to vary for the different spectra. In Fig. 6, we report the variation observed for the three free parameters.

In conclusion, from the NICER analysis, we confirm the presence of neutral variable absorption along the line of sight on short (∼1 day) timescales during the first and between each segment of the IXPE observation. The same variability, along with that of the X-ray photon index, is also evident when fitting *XMM* and *NuSTAR* data. This variability extends over long timescales. Indeed, the parameters of the continuum and absorbers show variation when compared to the data taken in 2022 (see Table 2). However, the overall adopted model appears to remain valid. Therefore, in the spectro-polarimetric analysis discussed in the next section, we used this model for the two IXPE campaigns, allowing these parameters to vary.

3.3. Spectro-polarimetric analysis: XMM-Newton, NuSTAR, and IXPE

The spectro-polarimetric analysis was conducted following the methodology presented in G23. i) We fit the IXPE data (I, Q, and
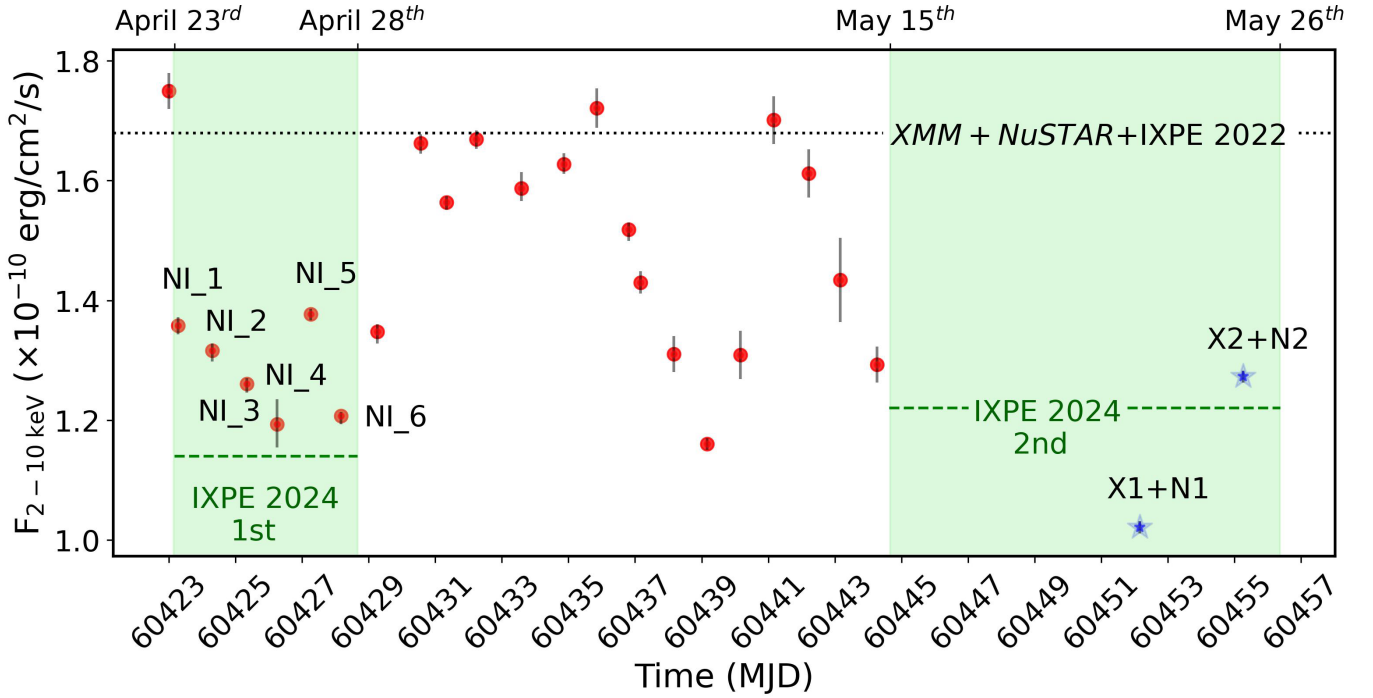
Fig. 5. Comparison between NICER and *XMM+NuSTAR* flux. The observed flux for the NICER daily monitoring of NGC 4151 is shown with red dots. The light green bands show the two segments of the IXPE pointing, and the dashed green lines are the respective extrapolated 2.0–10.0 keV fluxes. The blue stars are the flux values obtained for X1+N1 and X2+N2. The dotted black line represents the flux observed during the first observational campaign.
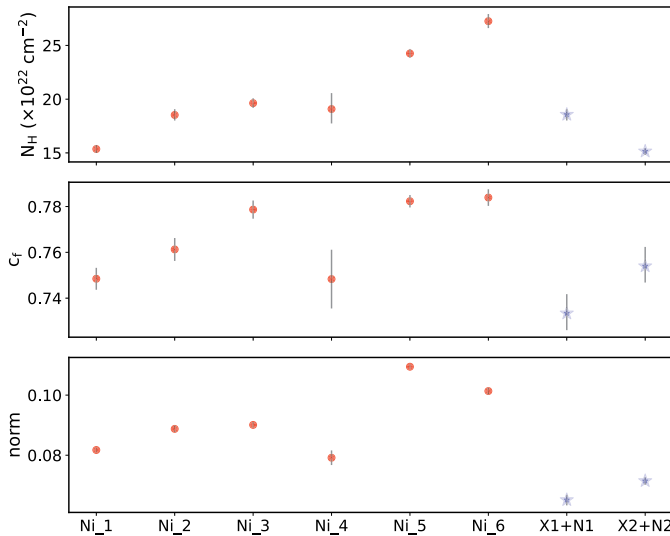

Fig. 6. Spectral parameter variability. We show the variations of the column density (upper panel) and covering factor (middle panel) of the first neutral partial covering along with those of the primary continuum normalization (lower panel) for the NICER data (red dots) and for *XMM+NuSTAR* (blue stars).

U spectra of the three detectors, for both observations; see Fig. 7) by applying the *XMM-Newton+NuSTAR* best fit (see Sec. 3.2). We included an inter-calibration constant between each detector (which were free to vary and of the order of ∼1.00). Given the variability reported in Sect. 3.2, we left to vary the primary continuum normalization and the parameters of the first neutral partial covering for the second observation (in comparison to those of the first observation that are set to the best fit values

derived in G23). ii) We added `polconst` multiplicative models in order to derive the polarization of each individual component. The PD and PA were set to zero for the `BORUS` table, accounting for the fluorescent lines and for the `CLOUDY` component (see G23). We note that the G23 spectro-polarimetric model considers a further spectral component with assigned `polconst`: the primary continuum leaking through the absorbers. By adopting the same configuration reported in the first paper (i.e., with the primary continuum and the reflection PAs forced to differ by 90° and PDs left free to vary while the PD and PA of the leaking emission were set to zero), we obtained a good fit (χ^2/ d.o.f = 1298/1222 for the 18 IXPE spectra) in which the polarization is attributed to the primary continuum, with $\Pi = 7.1 \pm 1.2\%$ and $\Psi = 84° \pm 5°$. Only an upper limit was derived for the reflection component $\Pi < 17\%$ (Model 1 in Table 3). As in G23, if the continuum and reflection PAs are set to be parallel (i.e., given a slab coronal geometry, the reflection is from the disk), the reflection component PD is unconstrained.

Despite the goodness of the above fit, an excess below 4 keV in the *Q* and *U* spectra was clearly visible (see Fig. 7, right panel). This excess drives the change in the PA in the 2.0–3.5 keV energy bin (see Sect. 3.1). Given the higher statistic from considering both observations, we attempted to simultaneously constrain the polarization properties of the leaking emission along with those of the X-ray continuum and of the reflection. Starting from the above spectro-polarimetric fit, we then allowed the PA and PD of the leakage to vary. Since we were unable to also constrain the polarimetric properties of the reflection component, we assumed it is either unpolarized or has PD = 20%, with a PA parallel or perpendicular to that of the primary continuum (see Table 3, Model 2 and Model 3). The statistical quality of the fit improved (down to χ^2/d.o.f = 1272/1221), with PD in the range ∼10−20% for both the primary continuum and the soft component in all cases and PAs of ∼100 and ∼20°, respectively.
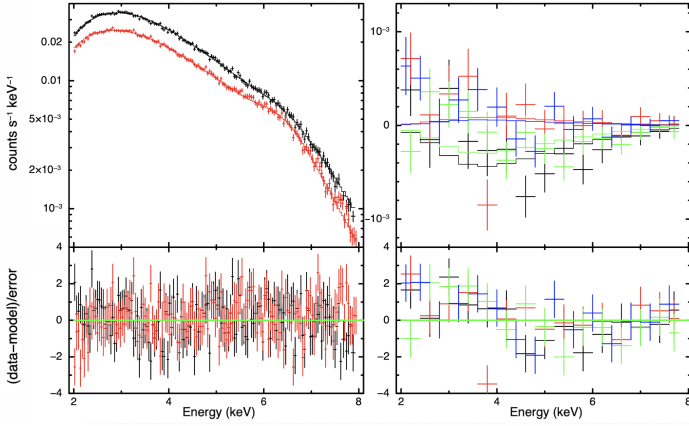
Fig. 7. IXPE spectra. Left panel: IXPE grouped Stokes I (in black the first and in red the second observation) spectra of NGC 4151 with residuals. Right panel: Q (in black the first and in green the second observation) and U (in red the first and in blue the second observation) grouped Stokes spectra are shown with residuals.

Table 3. Polarization degree and angle of each spectral component for different tests conducted during the spectro-polarimetric analysis.

Component	PD [%]	PA [deg]	χ^2/d.o.f.
	Model 1		
Primary continuum	7.1 ± 1.2	84 ± 5	
Soft emission	0^{fix}	–	1298/1222
Neutral reflection	<17	$PA_p \pm 90°$	
	Model 2		
Primary continuum	15.6 ± 2.3	99 ± 4	
Soft emission	13.1 ± 2.5	20 ± 6	1272/1221
Neutral reflection	0^{fix}	–	
	Model 3A		
Primary continuum	19.4 ± 2.3	100 ± 4	
Soft emission	14.4 ± 2.5	20 ± 5	1276/1221
Neutral reflection	20^{fix}	$PA_p \pm 90°$	
	Model 3B		
Primary continuum	11.8 ± 2.5	98 ± 4	
Soft emission	11.8 ± 2.5	20 ± 6	1274/1221
Neutral reflection	20^{fix}	PA_p	
	Model 4		
Primary continuum	7.0 ± 0.9	93 ± 4	
Soft emission	8.2 ± 2.2	22 ± 6	1287/1224
Neutral reflection	0^{fix}	–	

Notes. PA_p is the PA of the primary continuum.

We show in Fig. 8, the PD and PA as a function of energy, as predicted by the models described above and compared to the observed values, rebinned at 1 keV and grouped (all detectors for both observations) for a better visualization. Although these fits account for the switch of the PA in the soft X-rays, their physical interpretation is problematic. A PD of around 14% for the soft component may suggest that what we observed is not a leakage through the absorbing layers but rather the reflection of the primary emission on the inner accretion flow or on a mirror close to the disk. Concerning the primary emission, a Comptonizing X-ray corona cannot produce a PD in the 16-20% range. For instance, a slab corona, which produces the highest
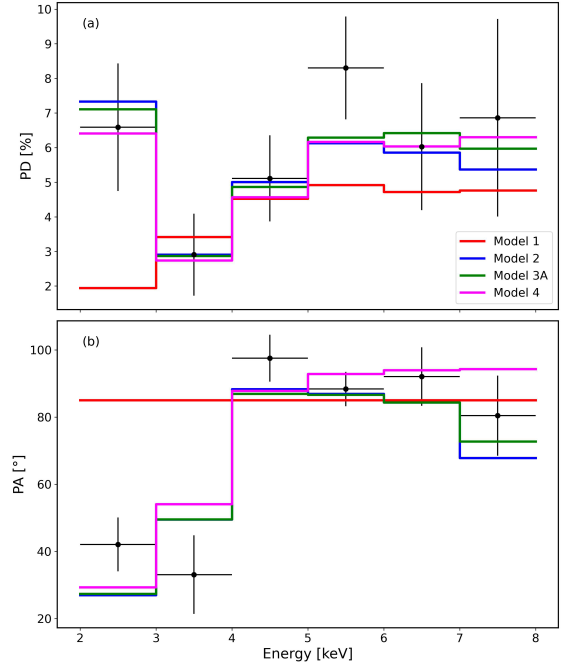

Fig. 8. Polarization properties as a function of energy. Panel a: Polarization degree. Panel b: Polarization angle. Referring to the models presented in Table 3, we show Model 1 in red, Model 2 in blue, Model 3A in green, and Model 4 in magenta. The IXPE spectra are rebinned at an interval of 1 keV.

PDs, can reach up to PD $\sim 12\%$, depending on the inclination (see Ursini et al. 2022).

In order to disentangle the coronal emission from the soft component, we tested a simplified phenomenological model composed only of a power law and a blackbody (with temperature ~ 0.5 keV) and with each obscured by a different layer of neutral matter (of the order of 10^{23} and 10^{22} cm^{-2}, respectively). The two components have separate polarization properties, while the Fe Kα line is considered unpolarized. From a statistical point of view, the fit is similar to the previous ones (χ^2/d.o.f. = 1287/1224). While still reproducing the angle switch at low energies, this model recovers a PD of $\sim 7\%$ for the primary emission, with a similar PD ($\sim 8\%$) for the soft component (Table 3, Model 4, and Fig. 8).

4. Discussion and conclusions

Our spectral analysis of the available *XMM-Newton*, *NuSTAR*, and NICER data of NGC 4151 (see Sect. 3.2) revealed variations in the absorbers and in the primary continuum compared to the 2022 data and between the two new sets of observations. Specifically, we observed variability in the X-ray photon index, continuum normalization, and both neutral and ionized absorbers along the line of sight on short (~ 1 day) and long (~ 1.5 year) timescales, suggesting ongoing dynamic processes in the source environment (see Figs. 5 and 6, and Table 2). Meanwhile, all the physical parameters of the reflection component are compatible with being constant with respect to the past data (see Table 2 and Fig. 4), so its contribution to the IXPE energy band is higher in the new observations (see Table 2).

Despite the lower flux state of NGC 4151 and the higher contribution of the reflection component, we find no evidence for variations in the observed polarization properties, with the PD and PA being in good agreement between the first and

second observations in all considered energy ranges (see the polarimetric analysis in Sect. 3.1). This allowed for an analysis of the combined observations, which yielded better constraints for PD and PA. In particular, in the full IXPE energy band (i.e., 2.0–8.0 keV), we obtained $\Pi = 4.5 \pm 0.9\%$ and $\Psi = 81° \pm 6°$. The latter aligns very well with the radio emission (see Fig. 2), which shows an average position angle of $\sim77-83°$ (e.g., Harrison et al. 1986; Ulvestad et al. 1998; Mundell et al. 2003; Williams et al. 2017, see Fig. 2). Furthermore, we confirm with a higher confidence (detected at $\sim3.5\sigma$ in the combined data versus $\sim2.2\sigma$ in the individual observations) the change in PA between the low energy bin (2.0–3.5 keV) and the higher bins (i.e., 3.5–5.0 keV and 5.0–8.0 keV) or the full band, already observed in G23 (see Table 1 and Fig. 1 and 2). Interestingly, the PA in this soft X-ray bin (i.e., $37° \pm 7°$) appears to align with an unclassified feature identified by Draper et al. (1992) that presents an enhanced extra-nuclear polarization in the I-band, located at $\sim17''$ from the center at position angles of $35°$ and $215°$ (see Fig. 2).

A spectro-polarimetric fit on both IXPE observations gave results in full agreement with what is presented in G23, albeit with more constrained PD and PA values (i.e., $\Pi = 7.1 \pm 1.2\%$ and $\Psi = 84° \pm 5°$) for the X-ray corona emission. As detailed in G23, these polarization properties are consistent with a slab or wedge geometry for the X-ray corona, as strongly reinforced by the alignment with the double-sided radio jet mentioned above.

However, in this spectro-polarimetric fit, an excess of the Q and U data with respect to the model is apparent below 4 keV (see Fig. 7), driving the clear change of PA at lower energies (see Fig. 2 and 8). This observational evidence suggests the presence of an additional soft X-ray component, which could be dominated by the leakage of the primary emission through the absorbers, as modeled in our spectroscopic best fit. We allowed the PA and PD of the leakage to vary, assuming that the reflection component is either unpolarized or has a PD of 20% with a PA parallel or perpendicular to the primary continuum (see Sect. 3.3). This improved the statistical quality of the spectro-polarimetric fit, notably modeling the PA switch at low energies (Table 3 and Fig. 8). The PD found for the soft component is fairly high (in the range of 12–14%), disfavoring the leakage hypothesis and rather suggesting scattering of the primary emission off the inner accretion flow or another mirror. In the latter case, this may suggest that the contribution of the NLR emission to the IXPE energy band is much larger than what is predicted by our best fit model as a result of an over-simplification of the very complex spectrum of NGC 4151 around 2 keV. However, the PA attributed to this component in these spectro-polarimetric fits is around $20°$, which is very distinct compared to the observed position angle of $\sim60°$ of the extended, biconical, NLR observed in near-IR, [O III] and X-rays (see, e.g., Draper et al. 1992; Wang et al. 2011; Marin et al. 2020, and references therein).

These fits yielded a higher PA for the primary continuum, around $100°$, which somewhat departs from the position angle of the radio emission, although sub-arcsecond resolution observations have shown that the inner ~150 pc of the radio jet is aligned with a PA of $\sim90°$ (Mundell et al. 2003). Moreover, as for the soft X-ray component, the derived PD for the primary continuum is very high (10–20%), challenging the interpretation of this component as the intrinsic coronal emission. Both issues are solved by completely disentangling the primary continuum from the soft component thanks to a simplified phenomenological model, composed only by a power-law and a blackbody. This suggests again that a significant part of the spectral complexity

around 2–3 keV is not due to leakage of the primary continuum but rather to an independent component.

We did not detect clear evidence of reflection off the accretion disk in the current data (see Sect. 3.2) nor in the 2022 spectra (see G23). However, we cannot rule out the possibility that a significant part of the X-ray polarization above ~4 keV is produced by disk reflection (see, e.g., Podgorný et al. 2022, 2023) without clear spectroscopic signatures. This scenario will be explored with a self-consistent spectro-polarimetric analysis in a forthcoming publication (Dovčiak et al., in preparation). We note here that observing NGC 4151 with IXPE in a much lower flux state could break this degeneracy and provide a more comprehensive understanding of the polarimetric properties of the AGN.

Data availability

The IXPE data used in this paper are publicly available in the HEASARC database (https://heasarc.gsfc.nasa.gov/docs/ixpe/archive/). The *XMM-Newton* and *NuSTAR* data are subject to an embargo of 12 months from the date of the observations. Once the embargo expires (May 31, 2025) the data will be publicly available from the *XMM-Newton* (http://nxsa.esac.esa.int/) and the *NuSTAR* (https://heasarc.gsfc.nasa.gov/docs/nustar/nustar_archive.html) archives. The NICER data are publicly available in the HEASARC database (https://heasarc.gsfc.nasa.gov/docs/nicer/nicer_archive.html).

References

Antonucci, R. R. J., & Cohen, R. D. 1983, ApJ, 271, 564
Arnaud, K. A. 1996, ASP Conf. Ser., 101, 17
Arzoumanian, Z., Gendreau, K. C., Baker, C. L., et al. 2014, SPIE Conf. Ser., 9144, 914420
Baldini, L., Bucciantini, N., Lalla, N. D., et al. 2022, SoftwareX, 19, 101194
Baloković, M., Brightman, M., Harrison, F. A., et al. 2018, ApJ, 854, 42
Baloković, M., García, J. A., & Cabral, S. E. 2019, Res. Notes Am. Astron. Soc., 3, 173
Bentz, M. C., Williams, P. R., & Treu, T. 2022, ApJ, 934, 168
Beuchert, T., Markowitz, A. G., Dauser, T., et al. 2017, A&A, 603, A50
Bianchi, S., Chiaberge, M., Evans, D. A., et al. 2010, MNRAS, 405, 553
De Rosa, A., Piro, L., Perola, G. C., et al. 2007, A&A, 463, 903
Di Marco, A., Costa, E., Muleri, F., et al. 2022, AJ, 163, 170
Di Marco, A., Soffitta, P., Costa, E., et al. 2023, AJ, 165, 143
Draper, P. W., Gledhill, T. M., Scarrott, S. M., & Tadhunter, C. N. 1992, MNRAS, 257, 309
Fabian, A. C., Lohfink, A., Kara, E., et al. 2015, MNRAS, 451, 4375

Fabian, A. C., Lohfink, A., Belmont, R., Malzac, J., & Coppi, P. 2017, MNRAS, 467, 2566

Ferland, G. J., Korista, K. T., Verner, D. A., et al. 1998, PASP, 110, 761

Gendreau, K. C., Arzoumanian, Z., & Okajima, T. 2012, SPIE Conf. Ser., 8443, 844313

Gendreau, K. C., Arzoumanian, Z., Adkins, P. W., et al. 2016, SPIE Conf. Ser., 9905, 99051H

Gianolli, V. E., Kim, D. E., Bianchi, S., et al. 2023, MNRAS, 523, 4468

Gianolli, V. E., Bianchi, S., Petrucci, P.-O., et al. 2024, Mem. Soc. Astron. It., 95, 27

Harrison, B., Pedlar, A., Unger, S. W., et al. 1986, MNRAS, 218, 775

Harrison, F. A., Craig, W. W., Christensen, F. E., et al. 2013, ApJ, 770, 103

Ingram, A., Ewing, M., Marinucci, A., et al. 2023, MNRAS, 525, 5437

Kaastra, J. S., & Bleeker, J. A. M. 2016, A&A, 587, A151

Kamraj, N., Brightman, M., Harrison, F. A., et al. 2022, ApJ, 927, 42

Kang, J.-L., & Wang, J.-X. 2022, ApJ, 929, 141

Keck, M. L., Brenneman, L. W., Ballantyne, D. R., et al. 2015, ApJ, 806, 149

Kraemer, S. B., Schmitt, H. R., & Crenshaw, D. M. 2008, ApJ, 679, 1128

Lubiński, P., Zdziarski, A. A., Walter, R., et al. 2010, MNRAS, 408, 1851

Marin, F., Le Cam, J., Lopez-Rodriguez, E., et al. 2020, MNRAS, 496, 215

Marin, F., Gianolli, V. E., Ingram, A., et al. 2024, Galaxies, 12, 4

Marinucci, A., Muleri, F., Dovciak, M., et al. 2022, MNRAS, 516, 5907

Matt, G., Baloković, M., Marinucci, A., et al. 2015, MNRAS, 447, 3029

May, D., Steiner, J. E., Menezes, R. B., Williams, D. R. A., & Wang, J. 2020, MNRAS, 496, 1488

Muleri, F. 2022, in Analysis of the Data from Photoelectric Gas Polarimeters, eds. C. Bambi, & A. Santangelo (Singapore: Springer Nature Singapore), 1

Mundell, C. G., Wrobel, J. M., Pedlar, A., & Gallimore, J. F. 2003, ApJ, 583, 192

NASA Heasarc 2014, HEAsoft: Unified Release of FTOOLS and XANADU, Astrophysics Source Code Library [record ascl:1408.004]

Petrucci, P. O., Haardt, F., Maraschi, L., et al. 2001, ApJ, 556, 716

Piconcelli, E., Jimenez-Bailón, E., Guainazzi, M., et al. 2004, MNRAS, 351, 161

Podgorný, J., Dovčiak, M., Marin, F., Goosmann, R., & Różańska, A. 2022, MNRAS, 510, 4723

Podgorný, J., Dovčiak, M., Goosmann, R., et al. 2023, MNRAS, 524, 3853

Ricci, C., Ho, L. C., Fabian, A. C., et al. 2018, MNRAS, 480, 1819

Schnittman, J. D., & Krolik, J. H. 2010, ApJ, 712, 908

Serafinelli, R., Marinucci, A., De Rosa, A., et al. 2023, MNRAS, 526, 3540

Serafinelli, R., De Rosa, A., Tortosa, A., et al. 2024, A&A, 690, A145

Shapiro, S. L., Lightman, A. P., & Eardley, D. M. 1976, ApJ, 204, 187

Shapovalova, A. I., Popovic, L. C., Collin, S., et al. 2012, Astron. Astrophys. Trans., 27, 429

Storchi-Bergmann, T., McGregor, P. J., Riffel, R. A., et al. 2009, MNRAS, 394, 1148

Strüder, L., Briel, U., Dennerl, K., et al. 2001, A&A, 365, L18

Sunyaev, R. A., & Titarchuk, L. G. 1980, A&A, 86, 121

Tagliacozzo, D., Marinucci, A., Ursini, F., et al. 2023, MNRAS, 525, 4735

Tamborra, F., Matt, G., Bianchi, S., & Dovčiak, M. 2018, A&A, 619, A105

Tortosa, A., Bianchi, S., Marinucci, A., Matt, G., & Petrucci, P. O. 2018, A&A, 614, A37

Ulvestad, J. S., Roy, A. L., Colbert, E. J. M., & Wilson, A. S. 1998, ApJ, 496, 196

Ursini, F., Matt, G., Bianchi, S., et al. 2022, MNRAS, 510, 3674

Wang, J., Fabbiano, G., Risaliti, G., et al. 2011, ApJ, 729, 75

Weaver, K. A., Mushotzky, R. F., Arnaud, K. A., et al. 1994, ApJ, 423, 621

Weisskopf, M. C., Soffitta, P., Baldini, L., et al. 2022, J. Astron. Telesc. Instrum. Syst., 8, 026002

Williams, D. R. A., McHardy, I. M., Baldi, R. D., et al. 2017, MNRAS, 472, 3842

Wolfinger, K., Kilborn, V. A., Koribalski, B. S., et al. 2013, MNRAS, 428, 1790

Yang, Y., Wilson, A. S., & Ferruit, P. 2001, ApJ, 563, 124

Yaqoob, T., Edelson, R., Weaver, K. A., et al. 1995, ApJ, 453, L81

Zdziarski, A. A., Johnson, W. N., & Magdziarz, P. 1996, MNRAS, 283, 193

Zdziarski, A. A., Poutanen, J., & Johnson, W. N. 2000, ApJ, 542, 703

Zhang, W., Dovčiak, M., & Bursa, M. 2019, ApJ, 875, 148

Zoghbi, A., Miller, J. M., & Cackett, E. 2019, ApJ, 884, 26

Życki, P. T., Done, C., & Smith, D. A. 1999, MNRAS, 309, 561

[1] Université Grenoble Alpes, CNRS, IPAG, 38000 Grenoble, France

[2] Dipartimento di Matematica e Fisica, Università degli Studi Roma Tre, Via della Vasca Navale 84, 00146 Roma, Italy

[3] ASI – Agenzia Spaziale Italiana, Via del Politecnico snc, 00133 Roma, Italy

[4] INAF – Astronomical Observatory of Rome, Via Frascati 33, 00040 Monte Porzio Catone, Italy

[5] INAF Istituto di Astrofisica e Planetologia Spaziali, Via del Fosso del Cavaliere 100, I-00133 Roma, Italy

[6] Dipartimento di Fisica, Università degli Studi di Roma "La Sapienza", Piazzale Aldo Moro 5, I-00185 Roma, Italy

[7] Dipartimento di Fisica, Università degli Studi di Roma "Tor Vergata", Via della Ricerca Scientifica 1, I-00133 Roma, Italy

[8] Université de Strasbourg, CNRS, Observatoire Astronomique de Strasbourg, UMR 7550, 67000 Strasbourg, France

[9] Centre for Extragalactic Astronomy, Department of Physics, University of Durham, South Road, Durham DH1 3LE, UK

[10] Institute of Space and Astronautical Science (ISAS), Japan Aerospace Exploration Agency (JAXA), Kanagawa 252-5210, Japan

[11] MIT Kavli Institute for Astrophysics and Space Research, Massachusetts Institute of Technology, 77 Massachusetts Avenue, Cambridge, MA 02139, USA

[12] Space Science Data Center, Agenzia Spaziale Italiana, Via del Politecnico snc, 00133 Roma, Italy

[13] Astronomical Institute of the Czech Academy of Sciences, Bocří II 1401/1, 14100 Praha 4, Czech Republic

[14] Istituto Nazionale di Fisica Nucleare, Sezione di Roma "Tor Vergata", Via della Ricerca Scientifica 1, 00133 Roma, Italy

[15] Department of Astronomy, University of Maryland, College Park, Maryland 20742, USA